Observation of Anisotropic Dispersive Dark-Exciton Dynamics in CrSBr

J. Sears,[1] B. Zager,[1,2] W. He,[1,*] C. A. Occhialini,[2,3] Y. Shen,[1,†,‖] M. Lajer,[1] J. W. Villanova,[4,‡] T. Berlijn,[4] F. Yakhou-Harris,[5] N. B. Brookes,[5] D. G. Chica,[6] X. Roy,[6] E. Baldini,[7] J. Pelliciari,[2] V. Bisogni,[2] S. Johnston,[8,9] M. Mitrano,[10] and M. P. M. Dean[1,§]

[1]*Department of Condensed Matter Physics and Materials Science, Brookhaven National Laboratory, Upton, New York 11973, USA*
[2]*National Synchrotron Light Source II, Brookhaven National Laboratory, Upton, New York 11973, USA*
[3]*Department of Physics, Columbia University, New York, New York 10027, USA*
[4]*Center for Nanophase Materials Sciences, Oak Ridge National Laboratory, Oak Ridge, Tennessee 37831, USA*
[5]*European Synchrotron Radiation Facility (ESRF), B.P. 220, F-38043 Grenoble Cedex, France*
[6]*Chemistry Department, Columbia University, New York, New York 10027, USA*
[7]*Department of Physics, The University of Texas at Austin, Austin, Texas 78712, USA*
[8]*Department of Physics and Astronomy, The University of Tennessee, Knoxville, Tennessee 37966, USA*
[9]*Institute for Advanced Materials and Manufacturing, The University of Tennessee, Knoxville, Tennessee 37996, USA*
[10]*Department of Physics, Harvard University, Cambridge, Massachusetts 02138, USA*

(Received 23 September 2024; revised 19 June 2025; accepted 5 September 2025; published 1 October 2025)

Many-body excitons in CrSBr are attracting intense interest in view of their highly anisotropic magneto-optical coupling and their potential for novel optical interfaces within spintronic and magnonic devices. Characterizing the orbital character and propagation of these electronic excitations is crucial for understanding and controlling their behavior; however, this information is challenging to access. High resolution resonant inelastic x-ray scattering is a momentum-resolved technique that can address these crucial questions. We present measurements collected at the Cr L_3-edge which show a rich spectrum of excitations with a variety of spin-orbital characters. While most of these excitations appear to be localized, the dispersion of the lowest energy dark exciton indicates that it is able to propagate along both the a and b directions within the planes of the crystal. This two-dimensional character is surprising as it contrasts with electrical conductivity and the behavior of the bright exciton, both of which are strongly one dimensional. The discovery of this propagating dark exciton highlights an unusual coexistence of one- and two-dimensional electronic behaviors in CrSBr.

DOI: 10.1103/fz3h-6jdx

Introduction—The weak dielectric screening intrinsic to two-dimensional (2D) van der Waals (vdW) materials promotes the formation of strongly bound excitons, quasiparticles consisting of a bound electron and hole pair. Excitons often dominate the optical response in these materials and have for this reason been intensively studied for potential optoelectronics applications [1–3]. Optically forbidden dark excitons are highly sensitive to the electronic states of their host material [2,4] and are of interest for applications exploiting exciton coherence [5]. More recently, a variety of magnetic vdW materials have been reported [6,7] with the potential to support excitons with intertwined electronic and magnetic properties. Resonant inelastic x-ray scattering (RIXS) is a versatile measurement technique that can detect these various types of electronic excitation and provide information on their spin and orbital character not available from other techniques. RIXS also provides information about the exciton dispersion at nonzero momentum transfer, therefore probing the propagation of these excitations in the material [8]. This type of in-depth characterization will be valuable for understanding and tuning functional excitons for incorporation into devices.

CrSBr is a vdW material that was recently found to be magnetic down to the monolayer limit [9], and it possesses several other desirable properties for embedding into electronic and magnetic devices. It is semiconducting with a direct band gap of ∼1.8 eV, air stable, and has a relatively high bulk ordering temperature of $T_N \approx 132$ K [10–14].

*Present address: Stanford Institute for Materials and Energy Sciences, SLAC National Accelerator Laboratory, Menlo Park, California 94025, USA.
†Present address: Beijing National Laboratory for Condensed Matter Physics, Institute of Physics, Chinese Academy of Sciences, Beijing 100190, China.
‡Present address: Department of Physics and Astronomy, Middle Tennessee State University, Murfreesboro, Tennessee 37132, USA.
§Contact author: mdean@bnl.gov
‖School of Physical Sciences, University of Chinese Academy of Sciences, Beijing 100049, China.

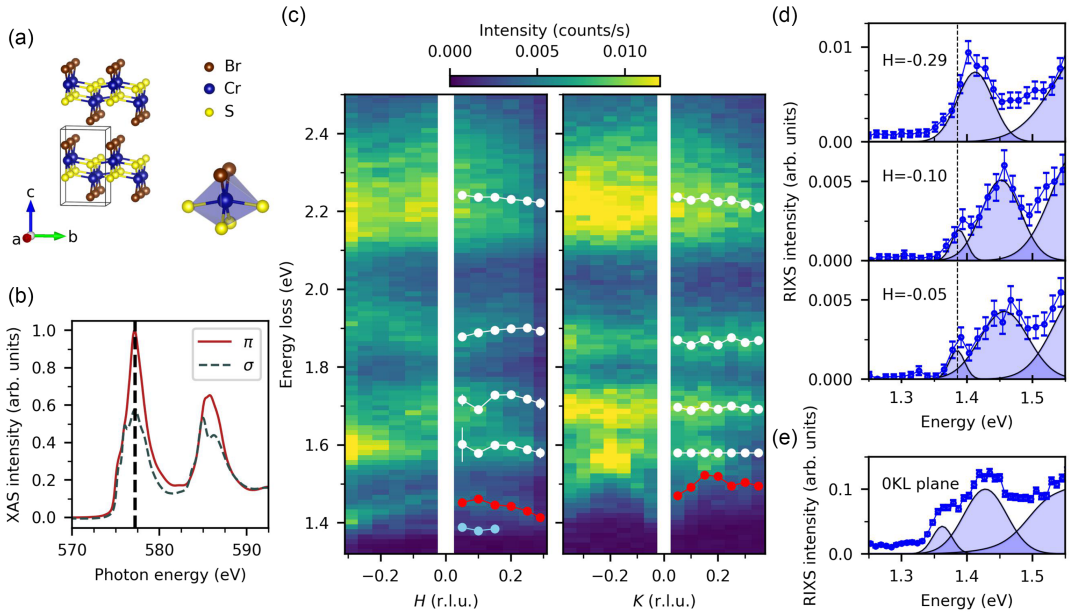

FIG. 1. Anisotropic dispersive exciton behavior in CrSBr. (a) Crystal structure. The gray cuboid shows the unit cell and the translucent blue octahedron shows the Cr coordination. (b) X-ray absorption measured in TFY mode as a function of incident photon energy, showing peaks at the Cr L_3 and L_2 edges. The data were collected in the $H0L$ plane, with an incident angle of $\theta_i = 45°$ and a scattering angle of $2\Theta = 90°$. The dashed vertical line indicates the energy at which the RIXS spectra in (c) were collected. σ polarization indicates vertical linear polarization of the incoming beam along the sample b axis, and π denotes horizontal linear polarization in the sample $a-c$ plane. (c) Exciton propagation along the H and K directions of the Brillouin zone. The peak positions extracted from the fit are plotted on one half of the data in each plane, showing nondispersive behavior in most of the excitons (white), as well as dispersive propagating behavior in one of the low-energy excitons (red). A nondispersive low energy feature, which we identify as the previously reported optically active exciton, is visible at low momentum transfers in the $H0L$ plane (blue). The H dependent measurements were collected at $K = 0$, with the beam polarization in the $H0L$ scattering plane. The K dependent measurements were collected at $H = 0$, with the photon polarization along the H axis perpendicular to the $0KL$ scattering plane. (d) Line cuts showing raw spectra and Gaussian fits to the low energy excitations in the $H0L$ plane, demonstrating that two peaks can be resolved in the 1.3 to 1.5 eV energy range. The vertical dashed line marks the position of the 1.38(1) eV feature. (e) Additional data measured with the sample in the $0KL$ plane at $K = 0$, demonstrating that the weak feature can also be resolved at sufficiently low momentum transfers.

Optical studies have identified a bright exciton at 1.37 eV, which shows a strong coupling with magnetism [15,16]. This discovery has prompted a great deal of research investigating the potential for optical control and detection of electronic and magnetic quasiparticle excitations in CrSBr [16–18].

The bright exciton in CrSBr is understood to have a delocalized character and to arise from hybridization between the Cr $3d$ and S and Br p states [15]. Although prior studies have reported a number of optically bright features in the 1.3–1.4 eV energy range, these result from coupling either to phonons or polariton modes [19–21]. The bare exciton energy has been found to be 1.37 eV in Ref. [20]. Photoluminesence measurements of the exciton show a striking anisotropy, with the exciton only visible when the light is polarized along the crystallographic b axis [15,22]. The exciton is consequently considered one dimensional (1D). This is a consequence of the highly anisotropic band structure, which results in quasi-1D electronic conduction along the b axis and localization along the a axis. The 1D electronic behavior is counterintuitive but understandable through a careful inspection of the crystal structure [10] shown in Fig. 1(a), which is made up of apparently well-connected bilayers of distorted CrS_4Br_2 octahedra. The electronic anisotropy is due to the Cr-ligand-Cr bond angles, which are ~90° along a and ~180° along b. The quasi-1D electronic conduction occurs along the nearly straight chains of Cr and S running along the b direction [22,23].

Here we present the first use of RIXS to determine the electronic character and propagation of excitons in CrSBr. We observed an exciton at 1.38(1) eV consistent with the previously reported bright exciton at 1.37 eV [20] and found that its changes with momentum are consistent with those expected for a 1D delocalized exciton [23]. We also detected several previously unreported excitations with higher energies up to 2.5 eV, including a dark exciton at 1.45 eV. While the higher-energy excitations are non-dispersing, indicating localized electronic character, the lowest-energy dark exciton at 1.45 eV shows more exotic behavior. This excitation shows a strong temperature dependence and an unusual 2D dispersion more consistent with local exchange hopping than with a strongly

delocalized exciton. The 2D nature of this propagating dark exciton contrasts with the generally 1D electronic behavior, highlighting the complex interplay between the 1D and 2D phenomena in CrSBr.

Methods—Single crystals of CrSBr were synthesized and aligned as described in Supplemental Material Sec. I [24]. Cr L_3-edge RIXS measurements were performed at the ID32 beam line of the European Synchrotron Radiation Facility (ESRF) [25]. σ polarization indicates vertical linear polarization of the incoming beam (perpendicular to the scattering plane), and π denotes horizontal linear polarization (in the scattering plane). Unless otherwise specified, a sample temperature of 30 K was used. The spectrometer was operated with a resolution of 30 meV for the reciprocal space maps and temperature dependence. Additional spectra [Figs. 1(e) and 2(b)] were collected at the SIX 2-ID beamline of the National Synchrotron Light Source II. The spectrometer was operated with a resolution of 28 meV. The CrSBr data were interpreted using the EDRIXS software as described in the End Matter [8,26,27].

Results and interpretation—We used RIXS to measure the electronic excitations and their momentum dynamics in CrSBr, with the incident photon energy tuned to the peak of the chromium L_3 x-ray absorption spectroscopy (XAS) spectrum. The Cr $L_{2,3}$ XAS measurements collected with horizontal (π) and vertical (σ) incident beam polarizations are shown in Fig. 1(b). These data were collected below the magnetic ordering temperature and consequently show dichroism due to crystallographic and magnetic symmetry breaking.

The RIXS spectra collected at the L_3 edge show several features between 1.3 and 2.5 eV energy loss, corresponding to different electronic excitations within the chromium d orbitals and hybridized ligand (S and Br) states. In Fig. 1(c) we show the momentum dependence of these excitations as a function of the H and K reciprocal space directions (CrSBr is a highly 2D material, so no variation is expected in L [12]). No features were observed in the RIXS spectra below 1.3 eV other than a shoulder on the elastic line, which is likely to arise from low energy (< 100 meV) magnons and phonons [12]. At energies higher than 2.5 eV, no sharp features were seen [28].

Within the 1.3 to 2.5 eV range, we have fit the spectrum at each momentum transfer with a collection of Gaussian peaks as shown in Supplemental Material Sec. II [24]. The peak positions derived from these fits are plotted on the right side of each reciprocal space map. At most momentum transfers, we fit the spectra with five Gaussian peaks; however, an additional weak peak was seen at low energy in the low momentum transfer region of the H direction reciprocal space map. The position of this peak [1.38 (1) eV] is marked by the blue points in Fig. 1(c) and agrees well with the 1.37 eV energy reported for the exciton in optical measurements [20], so we identify this as the optically active excitation that has been extensively studied

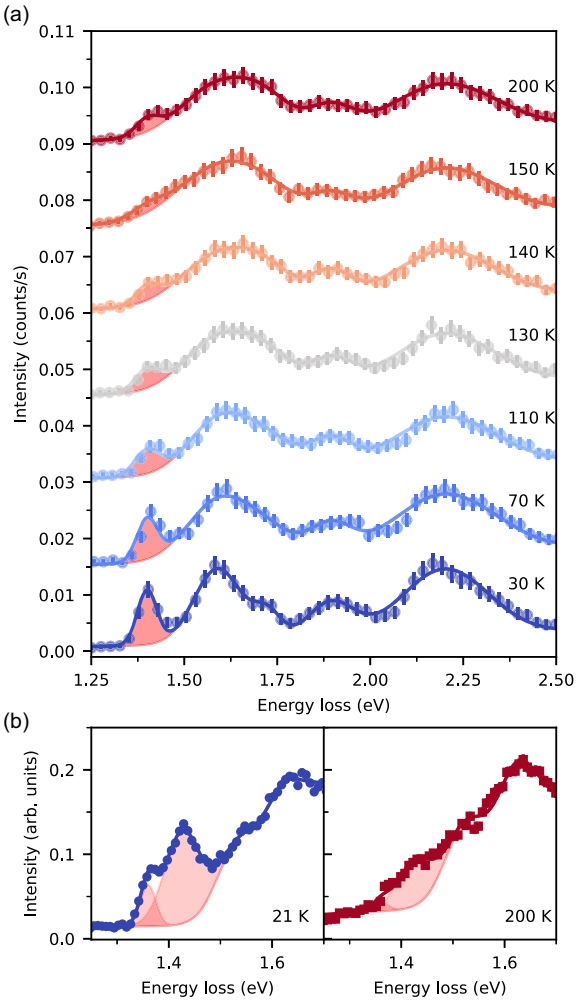

FIG. 2. Low-temperature emergence of excitons in CrSBr. (a) RIXS spectra with varying temperature, collected at 577.2 eV (L_3 edge) at $\theta_i = 9.4°$ and $2\Theta = 149°$. The prominent excitation visible at ~1.4 eV is the dark dispersive exciton and is highlighted by the pink shading at low temperature. This feature becomes weaker and broader with increasing temperature. The spectra were fit with five Gaussian functions with temperature-dependent widths and intensity and constant energies. (b) Temperature dependence measured at lower momentum transfer to resolve the two low energy peaks. The optically active and the dark dispersive excitons both show a similar decrease in intensity at higher temperatures above T_N. This data was collected at $\theta_i = 68.5°$ and $2\Theta = 150°$. Data in both panels was collected in the $H0L$ plane with a π-polarized beam.

in the literature. Figure 1(d) displays several spectra from this region as line cuts, which show more clearly the presence of this weak feature distinct from the higher energy excitations. The 1.38(1) eV peak is not seen in the K direction map, which is expected behavior for a band-edge excitation which would quickly disperse to higher energies in this direction due to the band anisotropy. It would then not be observable in our measurements since it would overlap with the higher energy excitations. We have

also collected an additional spectrum at $K = 0$, plotted in Fig. 1(e), showing that this excitation can be resolved in the $0KL$ scattering plane geometry at sufficiently small momentum transfers.

We find that most of the higher energy excitations do not show unambiguous dispersive behavior, with the exception of the low energy feature (1.46 eV at zero momentum transfer) marked by the red points. This excitation shows an intriguing asymmetry, dispersing downward along H and upward along K by a similar amount (∼50 meV). This type of dispersion is incompatible with a conventional particle-hole picture of the exciton, which would require a far larger exciton dispersive bandwidth (of order eV in magnitude) along b due to the larger conduction band dispersion in this direction, but it is compatible with an exciton that moves via exchange processes. This can be rationalized in view of bond-angle-dependent cancellation between different superexchange processes [29]. This type of cancellation is thought to be the mechanism behind the relatively isotropic magnon bandwidth [12]. Since this dispersive excitation has not been reported in optical measurements, we will refer to this as a "dark" exciton. We estimate the energy of the dark dispersive exciton to be 1.46(1) eV at zero momentum transfer, somewhat larger than the 1.38(1) eV energy observed for the bright exciton. The peak width was found to be 38(2) meV, slightly increased from the 30 meV resolution likely due to lifetime broadening. The peak width of the 1.38(1) eV bright exciton was resolution limited.

In Fig. 2(a) we show the temperature dependence at the momentum transfer $\vec{q} = (-0.29, 0, 0.28)$ reciprocal lattice units from the base temperature of 30 K up to 200 K, well above the magnetic ordering temperature of 132 K. We find that the dark dispersive excitation shows the largest change, nearly disappearing at the highest temperatures. While the 1.37 eV optically active exciton is not visible at this momentum transfer, we have collected additional spectra at smaller momentum transfer and found that the bright exciton shows a similar behavior at high temperature. These additional spectra are shown in Fig. 2(b). While the higher energy excitations become generally broader and weaker, they do not undergo the same loss in spectral weight.

To gain more insight into the nature of the electronic excitations, we simulated the RIXS spectra using a cluster model as described in the End Matter. RIXS has unique advantages for studying nominally optical dipole forbidden many-body excitons, as it couples to them directly via a well-known cross section. This stands in contrast to optics since the theoretical description of the optical cross section for these modes is an area of active research [30].

In our model, the hopping parameters for the simulation were fixed using first-principles calculations. Since the effective octahedral crystal field parameter $10Dq$, Hund's coupling J_H, and the charge-transfer energy Δ depend

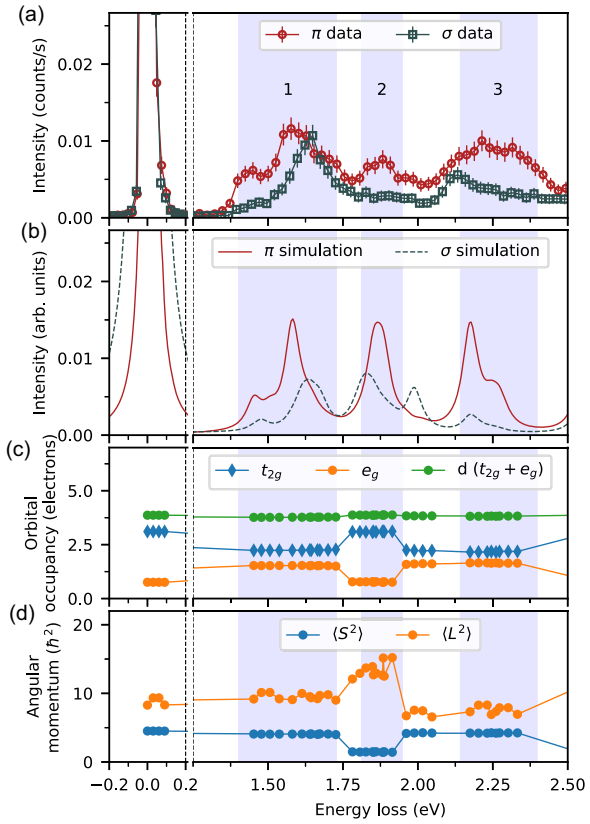

FIG. 3. Electronic character of the CrSBr excitons. (a) Low-temperature (30 K) RIXS spectra collected in the $H0L$ plane at $\theta_i = 15°$, $2\Theta = 90°$, and 577.4 eV. (b) AIM simulations that capture the main structures and polarization dependence observed in RIXS. (c),(d) Plot of the orbital occupancies and spin and orbital angular momentum expectation values squared, denoted as $\langle S^2 \rangle$ and $\langle L^2 \rangle$, respectively. We identify three manifolds of excitations: $t_{2g} \rightarrow e_g$ excitations below 1.75 eV, high spin-to-low-spin excitations from 1.75–2 eV, and second manifold of $t_{2g} \rightarrow e_g$ excitations with reduced orbital angular momentum L above 2 eV.

sensitively on electron-electron interactions, we followed typical analysis approaches for RIXS [31] and treated these as free parameters to fit the data. We also adjusted the crystal field levels of the individual t_{2g} orbitals to reproduce the splitting seen in the lowest energy manifold (1.4–1.7 eV). The results of the model shown in Fig. 3 represent the best match to the intensities at this momentum transfer.

The results of this modeling are shown in Fig. 3(b), along with the measured spectra in Fig. 3(a). The model can reproduce the energies of the main three features [labeled 1, 2, and 3 in Fig. 3(a)] at ∼1.6, 1.8, and 2.3 eV energy loss. The position of peak 1 was found to depend primarily on $10Dq$, and peak 2 was on J_H. Once these two parameters were fixed, the value of Δ was adjusted to give the best match for the energy of peak 3. The resultant parameters are all physically reasonable. The Coulomb interactions

correspond to a 70% screening with respect to atomic values, which is typical for transition metals [32]. The small value for the charge transfer energy reaffirms angle-resolved photoemission and density functional theory (DFT) predictions of strong mixing between Cr and S/Br at the Fermi level [33], and the crystal field values are of a comparable magnitude to other vdW materials [34–39].

The ground state of the model is high-spin $S \approx 3/2$ with strong ligand character and mixing between d^3, $d^4\underline{L}$, and $d^5\underline{L}^2$ configurations, where $\underline{L}$ denotes a ligand hole. The different excitations can be identified by computing the orbital occupancies, as well as the spin and orbital magnetic moment expectation values for our Anderson impurity model (AIM). These results are shown in Figs. 3(c) and 3(d), which show that the lowest energy manifold of excitations has a primarily $t_{2g} \rightarrow e_g$ character. This is indicated by the change in occupancy of the t_{2g} and e_g levels compared to the ground state, with no change in the spin or orbital moments. While we cannot unambiguously identify the individual subpeaks within feature 1, all excitations within this energy range have $t_{2g} \rightarrow e_g$ character. Feature 2 has instead a Hund's character, where t_{2g} occupancy remains the same but total spin is reduced. The highest energy manifold of excitations (peak 3) also has $t_{2g} \rightarrow e_g$ character, but with a reduced value of the total orbital angular momentum. This reflects the increased contribution of the $t_{2g} \rightarrow e_g$ transitions with higher Coulomb energy cost.

The predicted character of the lowest energy, dark dispersive exciton is of particular interest. In view of the dispersive nature of the low energy modes, it is clear that they have particularly extended character, so they cannot be completely described by the cluster model. Our modeling nonetheless indicates that the low-energy excitons must have $t_{2g} \rightarrow e_g$ character. This distinguishes CrSBr from some other excitons in vdW materials such as $NiPS_3$, which host an exciton that involves a high-spin to low-spin transition within the same orbital manifold [35,36]. To move the spin-flip excitation down to the observed energy of the dispersive exciton, the J_H parameter must be reduced to unphysically small values where the Slater (Coulomb interaction) parameters are scaled down to approximately half of their atomic values. This is below the range of values that are considered physically reasonable [32].

Conclusions—Our RIXS measurements of electronic excitations in CrSBr allowed us to characterize the momentum dependence of the full complement of electronic excitations, including optically dark excitons not previously reported. The coexistence of 2D dark excitons and 1D bright excitons may open long-term routes to control the directionality of exciton transport by exciting CrSBr at different energies [40], and dark excitons offer possibilities for modifying the optical activity of these excitons in search of future coherence applications [2,4,5]. Comparing the measured spectra with the model results also allows us to determine the essential orbital and spin character of these excitons, providing a comprehensive characterization of the electronic excitations in this candidate functional material.

We detect the previously reported bright exciton at 1.38(1) eV but also find a rich spectrum including a number of dark excitons at higher energies. The bright exciton shows the momentum dependence expected for a highly one-dimensional band-edge excitation, while most of the dark excitons do not disperse. However, the lowest energy dark exciton [1.46 eV at the Brillouin zone center and 1.4 eV at $\vec{q} = (-0.29, 0, 0.28)$] exhibits more exotic behavior, namely a strong temperature dependence and an anisotropic dispersion. This excitation disperses downward along H and upward along K, both with a similar $\sim$50 meV bandwidth. Such a dispersion is not compatible with a conventional strongly delocalized exciton, but suggests that this excitation propagates via exchange processes.

Our simulations using a cluster model allow us to assign the character of the various observed excitons. We find that the lowest energy (< 1.8 eV) excitations involve excitation of t_{2g} electrons to the e_g levels. The Hund's coupling has a slightly higher energy scale, leading to a peak in the RIXS spectrum at 1.9 eV, where the excited state involves a spin flip of one of the t_{2g} electrons. We conclude that the anisotropic dispersing dark exciton that we observe at 1.46 eV most likely has this $t_{2g} \rightarrow e_g$ orbital character and does not involve a spin flip. The discovery of this unusual exciton underlines the coexistence of 1D and 2D behavior in CrSBr.

Crystal structures were rendered using VESTA [41].

Acknowledgments—Work at Brookhaven and Harvard is supported by the Office of Basic Energy Sciences, Materials Sciences and Engineering Division, U.S. Department of Energy (DOE) under Contract No. DE-SC0012704. Work at the University of Tennessee (RIXS calculations and interpretation by model Hamiltonian calculations) was supported by the U.S. Department of Energy, Office of Science, Office of Basic Energy Sciences, under Award No. DE-SC0022311. E. B. was supported by the United States Army Research Office (W911NF-23-1-0394). Synthesis work at Columbia University was supported by the Programmable Quantum Materials, an Energy Frontier Research Center funded by the U.S. Department of Energy (DOE), Office of Science, Basic Energy Sciences (BES), under Award No. DESC0019443. This research used ESRF beam line ID32 under proposal HC5030. Part of this research (T. B.) was conducted at the Center for Nanophase Materials Sciences, which is a DOE Office of Science User Facility. The work by J. W. V. is supported by the Quantum Science Center (QSC), a National Quantum Information Science Research Center of DOE. We also acknowledge resources made available through BNL/LDRD#19-013. This research used beamline

2-ID of the National Synchrotron Light Source II, a U.S. DOE Office of Science User Facility operated for the DOE Office of Science by Brookhaven National Laboratory under Contract No. DE-SC0012704.

Data availability—The supporting data for the plots in this article are openly available from the Zenodo database [42].

[1] G. Wang, A. Chernikov, M. M. Glazov, T. F. Heinz, X. Marie, T. Amand, and B. Urbaszek, Colloquium: Excitons in atomically thin transition metal dichalcogenides, Rev. Mod. Phys. **90**, 021001 (2018).

[2] T. Mueller and E. Malic, Exciton physics and device application of two-dimensional transition metal dichalcogenide semiconductors, npj 2D Mater. Appl. **2**, 29 (2018).

[3] N. P. Wilson, W. Yao, J. Shan, and X. Xu, Excitons and emergent quantum phenomena in stacked 2D semiconductors, Nature (London) **599**, 383 (2021).

[4] M. R. Molas, C. Faugeras, A. O. Slobodeniuk, K. Nogajewski, M. Bartos, D. M. Basko, and M. Potemski, Brightening of dark excitons in monolayers of semiconducting transition metal dichalcogenides, 2D Mater. **4**, 021003 (2017).

[5] J. Zhu, Y. Li, X. Lin, Y. Han, and K. Wu, Coherent phenomena and dynamics of lead halide perovskite nanocrystals for quantum information technologies, Nat. Mater. **23**, 1027 (2024).

[6] K. S. Burch, D. Mandrus, and J.-G. Park, Magnetism in two-dimensional van der Waals materials, Nature (London) **563**, 47 (2018).

[7] Q. H. Wang *et al.*, The magnetic genome of two-dimensional van der Waals materials, ACS Nano **16**, 6960 (2022).

[8] M. Mitrano, S. Johnston, Y.-J. Kim, and M. P. M. Dean, Exploring quantum materials with resonant inelastic x-ray scattering, Phys. Rev. X **14**, 040501 (2024).

[9] K. Lee, A. H. Dismukes, E. J. Telford, R. A. Wiscons, J. Wang, X. Xu, C. Nuckolls, C. R. Dean, X. Roy, and X. Zhu, Magnetic order and symmetry in the 2D semiconductor CrSBr, Nano Lett. **21**, 3511 (2021).

[10] O. Goser, W. Paul, and H. G. Kahle, Magnetic properties of CrSBr, J. Magn. Magn. Mater. **92**, 129 (1990).

[11] E. J. Telford, A. H. Dismukes, K. Lee, M. Cheng, A. Wieteska, A. K. Bartholomew, Y.-S. Chen, X. Xu, A. N. Pasupathy, X. Zhu, C. R. Dean, and X. Roy, Layered antiferromagnetism induces large negative magnetoresistance in the van der Waals semiconductor CrSBr, Adv. Mater. **32**, 2003240 (2020).

[12] A. Scheie, M. Ziebel, D. G. Chica, Y. J. Bae, X. Wang, A. I. Kolesnikov, X. Zhu, and X. Roy, Spin waves and magnetic exchange Hamiltonian in CrSBr, Adv. Sci. **9**, 2202467 (2022).

[13] M. E. Ziebel, M. L. Feuer, J. Cox, X. Zhu, C. R. Dean, and X. Roy, CrSBr: An air-stable, two-dimensional magnetic semiconductor, Nano Lett. **24**, 4319 (2024).

[14] S. Smolenski, M. Wen, Q. Li, E. Downey, A. Alfrey, W. Liu, A. L. N. Kondusamy, A. Bostwick, C. Jozwiak, E. Rotenberg, L. Zhao, H. Deng, B. Lv, D. Zgid, E. Gull, and N. H. Jo, Large exciton binding energy in a bulk van der Waals magnet from quasi-1D electronic localization, Nat. Commun. **16**, 1134 (2025).

[15] N. P. Wilson, K. Lee, J. Cenker, K. Xie, A. H. Dismukes, E. J. Telford, J. Fonseca, S. Sivakumar, C. Dean, T. Cao, X. Roy, X. Xu, and X. Zhu, Interlayer electronic coupling on demand in a 2D magnetic semiconductor, Nat. Mater. **20**, 1657 (2021).

[16] Y. J. Bae, J. Wang, A. Scheie, J. Xu, D. G. Chica, G. M. Diederich, J. Cenker, M. E. Ziebel, Y. Bai, H. Ren, C. R. Dean, M. Delor, X. Xu, X. Roy, A. D. Kent, and X. Zhu, Exciton-coupled coherent magnons in a 2D semiconductor, Nature (London) **609**, 282 (2022).

[17] G. M. Diederich, J. Cenker, Y. Ren, J. Fonseca, D. G. Chica, Y. J. Bae, X. Zhu, X. Roy, T. Cao, D. Xiao, and X. Xu, Tunable interaction between excitons and hybridized magnons in a layered semiconductor, Nat. Nanotechnol. **18**, 23 (2023).

[18] F. Dirnberger, J. Quan, R. Bushati, G. M. Diederich, M. Florian, J. Klein, K. Mosina, Z. Sofer, X. Xu, A. Kamra, F. J. García-Vidal, A. Alù, and V. M. Menon, Magneto-optics in a van der Waals magnet tuned by self-hybridized polaritons, Nature (London) **620**, 533 (2023).

[19] K. Lin, X. Sun, F. Dirnberger, Y. Li, J. Qu, P. Wen, Z. Sofer, A. Söll, S. Winnerl, M. Helm, S. Zhou, Y. Dan, and S. Prucnal, Strong exciton–phonon coupling as a fingerprint of magnetic ordering in van der Waals layered CrSBr, ACS Nano **18**, 2898 (2024).

[20] T. Wang, D. Zhang, S. Yang, Z. Lin, Q. Chen, J. Yang, Q. Gong, Z. Chen, Y. Ye, and W. Liu, Magnetically-dressed CrSBr exciton-polaritons in ultrastrong coupling regime, Nat. Commun. **14**, 5966 (2023).

[21] Y. Shao *et al.*, Magnetically confined surface and bulk excitons in a layered antiferromagnet, Nat. Mater. **24**, 391 (2025).

[22] F. Wu, I. Gutiérrez-Lezama, S. A. López-Paz, M. Gibertini, K. Watanabe, T. Taniguchi, F. O. von Rohr, N. Ubrig, and A. F. Morpurgo, Quasi-1D electronic transport in a 2D magnetic semiconductor, Adv. Mater. **34**, 2109759 (2022).

[23] J. Klein *et al.*, The bulk van der Waals layered magnet CrSBr is a quasi-1D material, ACS Nano **17**, 5316 (2023).

[24] See Supplemental Material at http://link.aps.org/supplemental/10.1103/fz3h-6jdx for details of the sample growth and dispersion fitting.

[25] N. Brookes, F. Yakhou-Harris, K. Kummer, A. Fondacaro, J. Cezar, D. Betto, E. Velez-Fort, A. Amorese, G. Ghiringhelli, L. Braicovich, R. Barrett, G. Berruyer, F. Cianciosi, L. Eybert, P. Marion, P. van der Linden, and L. Zhang, The beamline ID32 at the ESRF for soft x-ray high energy resolution resonant inelastic x-ray scattering and polarisation dependent x-ray absorption spectroscopy, Nucl. Instrum. Methods Phys. Res., Sect. A **903**, 175 (2018).

[26] Y. Wang, G. Fabbris, M. Dean, and G. Kotliar, EDRIXS: An open source toolkit for simulating spectra of resonant inelastic x-ray scattering, Comput. Phys. Commun. **243**, 151 (2019).

[27] EDRIXS website, https://github.com/NSLS-II/edrixs (2024) (accessed: 2021-09-27).

[28] V. Porée, A. Zobelli, A. Pawbake, J. Regner, Z. Sofer, C. Faugeras, and A. Nicolaou, Resonant x-ray spectroscopies on chromium 3D orbitals in CrSBr, arXiv:2501.04751.
[29] J. Kanamori, Superexchange interaction and symmetry properties of electron orbitals, J. Phys. Chem. Solids **10**, 87 (1959).
[30] S. G. Louie, Y.-H. Chan, F. H. da Jornada, Z. Li, and D. Y. Qiu, Discovering and understanding materials through computation, Nat. Mater. **20**, 728 (2021).
[31] M. W. Haverkort, M. Zwierzycki, and O. K. Andersen, Multiplet ligand-field theory using Wannier orbitals, Phys. Rev. B **85**, 165113 (2012).
[32] F. de Groot and A. Kotani, *Core Level Spectroscopy of Solids* (CRC Press, Boca Raton, 2008).
[33] M. D. Watson, S. Acharya, J. E. Nunn, L. Nagireddy, D. Pashov, M. Rösner, M. van Schilfgaarde, N. R. Wilson, and C. Cacho, Giant exchange splitting in the electronic structure of A-type 2D antiferromagnet CrSBr, npj 2D Mater. Appl. **8**, 54 (2024).
[34] W. He, J. Sears, F. Barantani, T. Kim, J. W. Villanova, T. Berlijn, M. Lajer, M. A. McGuire, J. Pelliciari, V. Bisogni, S. Johnston, E. Baldini, M. Mitrano, and M. P. M. Dean, Dispersive dark excitons in van der Waals ferromagnet CrI_3, Phys. Rev. X **15**, 011042 (2025).
[35] W. He, Y. Shen, K. Wohlfeld, J. Sears, J. Li, J. Pelliciari, M. Walicki, S. Johnston, E. Baldini, V. Bisogni, M. Mitrano, and M. P. M. Dean, Magnetically propagating Hund's exciton in van der Waals antiferromagnet $NiPS_3$, Nat. Commun. **15**, 3496 (2024).
[36] S. Kang *et al.*, Coherent many-body exciton in van der Waals antiferromagnet $NiPS_3$, Nature (London) **583**, 785 (2020).
[37] S. Son, Y. Lee, J. H. Kim, B. H. Kim, C. Kim, W. Na, H. Ju, S. Park, A. Nag, K.-J. Zhou, Y.-W. Son, H. Kim, W.-S. Noh, J.-H. Park, J. S. Lee, H. Cheong, J. H. Kim, and J.-G. Park, Multiferroic-enabled magnetic-excitons in 2D quantum-entangled van der Waals antiferromagnet NiI_2, Adv. Mater. **34**, 2109144 (2022).
[38] C. A. Occhialini, Y. Tseng, H. Elnaggar, Q. Song, M. Blei, S. A. Tongay, V. Bisogni, F. M. F. de Groot, J. Pelliciari, and R. Comin, Nature of excitons and their ligand-mediated delocalization in nickel dihalide charge-transfer insulators, Phys. Rev. X **14**, 031007 (2024).
[39] C. A. Occhialini, L. Nessi, L. G. P. Martins, A. K. Demir, Q. Song, V. Hasse, C. Shekhar, C. Felser, K. Watanabe, T. Taniguchi, V. Bisogni, J. Pelliciari, and R. Comin, Spin-forbidden excitations in the magneto-optical spectra of cri_3 tuned by covalency, Phys. Rev. X **15**, 031005 (2025).
[40] E. Malic, R. Perea-Causin, R. Rosati, D. Erkensten, and S. Brem, Exciton transport in atomically thin semiconductors, Nat. Commun. **14**, 3430 (2023).
[41] K. Momma and F. Izumi, VESTA3 for three-dimensional visualization of crystal, volumetric and morphology data, J. Appl. Crystallogr. **44**, 1272 (2011).
[42] J. Sears, B. Zager, W. He, C. A. Occhialini, Y. Shen, M. Lajer, J. W. Villanova, T. Berlijn, F. Yakhou-Harris, N. B. Brookes, D. G. Chica, X. Roy, E. Baldini, J. Pelliciari, V. Bisogni, S. Johnston, M. Mitrano, and M. P. M. Dean, Data repsoitory for "Observation of anisotropic dispersive dark-exciton dynamics in CrSBr", https://doi.org/10.5281/zenodo.17132655.
[43] G. Kresse and J. Furthmüller, Efficient iterative schemes for *ab initio* total-energy calculations using a plane-wave basis set, Phys. Rev. B **54**, 11169 (1996).
[44] G. Kresse and J. Furthmüller, Efficiency of ab-initio total energy calculations for metals and semiconductors using a plane-wave basis set, Comput. Mater. Sci. **6**, 15 (1996).
[45] J. P. Perdew, K. Burke, and M. Ernzerhof, Generalized gradient approximation made simple, Phys. Rev. Lett. **77**, 3865 (1996).
[46] P. E. Blöchl, Projector augmented-wave method, Phys. Rev. B **50**, 17953 (1994).
[47] G. Kresse and D. Joubert, From ultrasoft pseudopotentials to the projector augmented-wave method, Phys. Rev. B **59**, 1758 (1999).
[48] A. A. Mostofi, J. R. Yates, G. Pizzi, Y.-S. Lee, I. Souza, D. Vanderbilt, and N. Marzari, An updated version of Wannier90: A tool for obtaining maximally-localised Wannier functions, Comput. Phys. Commun. **185**, 2309 (2014).
[49] N. Marzari and D. Vanderbilt, Maximally localized generalized Wannier functions for composite energy bands, Phys. Rev. B **56**, 12847 (1997).
[50] I. Souza, N. Marzari, and D. Vanderbilt, Maximally localized Wannier functions for entangled energy bands, Phys. Rev. B **65**, 035109 (2001).
[51] A. Bocquet, T. Saitoh, T. Mizokawa, and A. Fujimori, Systematics in the electronic structure of 3D transition-metal compounds, Solid State Commun. **83**, 11 (1992).
[52] S. Feldkemper and W. Weber, Generalized calculation of magnetic coupling constants for Mott-Hubbard insulators: Application to ferromagnetic Cr compounds, Phys. Rev. B **57**, 7755 (1998).
[53] R. D. Cowan, *The Theory of Atomic Structure and Spectra* (University of California Press, Berkeley, 1981).

End Matter

RIXS calculations—The CrSBr data were interpreted using exact diagonalization (ED) methods [8,26,27] based on an AIM constructed from the cluster shown in Fig. 1(a) in which the Cr atoms are surrounded by 4 S and 2 Br atoms. Similar methods have been successfully applied to several other vdW systems [34–39].

To determine the hopping parameters for our model, we first computed the electronic structure of CrSBr using the DFT code VASP [43,44]. The calculations are performed within the Perdew-Burke-Ernzerhof generalized gradient approximation [45] for the exchange-correlation functional without spin-orbit coupling. We use projector augmented wave pseudopotentials [46,47] with an energy cutoff of 450 eV and a $20 \times 14 \times 10$ Monkhorst-Pack k-point mesh. We constructed a tight-binding model using WANNIER90 [48–50] by performing a Wannier projection of

TABLE I. Input parameters for the four-fermion term. All numbers are in units of eV, with the exception of k_{dd} and k_{dp} which are scaling parameters. Bold denotes values tuned to match experiment.

Initial state										
d-d Coulomb interactions										
U_{dd}	k_{dd}	F^0_{dd}	F^2_{dd}	F^4_{dd}						
4	**0.72**	4.4	7.76	4.86						
Intermediate state										
d-d Coulomb interactions							*d-p* Coulomb interactions			
U_{dd}	k_{dd}	F^0_{dd}	F^2_{dd}	F^4_{dd}	U_{dp}	k_{dp}	F^0_{dp}	F^2_{dp}	G^1_{dp}	G^3_{dp}
4	**0.72**	4.43	8.35	5.23	6	0.7	6.31	4.57	3.35	1.91

Cr $3d$, S $3p$, and Br $4p$ orbitals without maximal localization.

The x, y, and z coordinate system used to describe the atomic and molecular orbitals are defined such that the axes point approximately along the bond directions. The z axis is along the crystallographic b axis, while x and y are in the $a-c$ plane and 45° rotated compared to the crystallographic axes. x is in the a, $c>0$ quadrant, and y is in the $a>0$, $c<0$ quadrant.

The Hamiltonian describing the cluster includes a four-fermion Coulomb term and a two-fermion term which includes contributions from crystal field, hopping, spin-orbit, and magnetic field. The diagonalization of the Hamiltonian, and calculation of the cross sections were performed using the Fortran AIM solver provided by EDRIXS package [26,27].

The four-fermion Coulomb term of the Hamiltonian includes interactions within the Cr $3d$ orbitals, as well as between the Cr $3d$ and Cr $2p$ orbitals in the intermediate state where a core hole is present. Coulomb interactions involving the ligand orbitals are expected to be relatively weak and so were not included. The Coulomb interactions for the Cr $3d$ orbitals can be described in terms of the Slater parameters F^0_{dd}, F^2_{dd}, and F^4_{dd}, while those between the Cr $3d$ and Cr $2p$ are parametrized by F^0_{dp}, F^2_{dp}, G^1_{dp}, and G^3_{dp}. Of these, F^0_{dd} and F^0_{dp} depend on the on-site Cr $3d$ Coulomb parameters U_{dd} and U_{dp}, which were set to typical values of 4 eV and 6 eV respectively [51,52]. The results of the simulation do not depend strongly on the precise values chosen. The rest of the parameters (F^2_{dd}, F^4_{dd}, F^2_{dp}, G^1_{dp}, and G^3_{dp}) were set to their Hartree-Fock atomic values calculated by Cowan's code [53], scaled down to account for screening effects in the crystal. One scaling factor was used for the Cr $3d$ orbitals, and one was for the core-hole interactions, denoted k_{dd} and k_{dp} respectively. k_{dp} does not strongly affect the fit to the experimental data, so it is fixed to 0.7. This leaves the scaling parameter k_{dd}, which is proportional to the Hund's coupling, as the only free parameter in the Coulomb portion of the Hamiltonian. All of the Coulomb parameters are listed in Table I.

The two-fermion term includes contributions from crystal field, hopping, spin-orbit coupling, and magnetic field. The crystal field and hopping terms are derived from the DFT calculation can be represented as a 10×10 matrix as follows

$$
\begin{array}{c}
\\
d_{x^2-y^2}\\
d_{3z^2-r^2}\\
d_{xy}\\
d_{xz}\\
d_{yz}\\
L_{x^2-y^2}\\
L_{3z^2-r^2}\\
L_{xy}\\
L_{xz}\\
L_{yz}
\end{array}
\begin{array}{c}
\begin{array}{cccccccccc}
d_{x^2-y^2} & d_{3z^2-r^2} & d_{xy} & d_{xz} & d_{yz} & L_{x^2-y^2} & L_{3z^2-r^2} & L_{xy} & L_{xz} & L_{yz}
\end{array}\\
\left(\begin{array}{cccccccccc}
3.201 & 0 & 0 & 0 & 0 & -2.426 & 0 & 0 & 0 & 0\\
0 & 3.227 & 0.0147 & 0 & 0 & 0 & -2.313 & -0.15 & 0 & 0\\
0 & 0.0147 & 2.662 & 0 & 0 & 0 & 0.159 & -1.49 & 0 & 0\\
0 & 0 & 0 & 2.733 & -0.041 & 0 & 0 & 0 & -1.383 & -0.068\\
0 & 0 & 0 & -0.041 & 2.733 & 0 & 0 & 0 & -0.068 & -1.383\\
-2.426 & 0 & 0 & 0 & 0 & 1.573 & 0 & 0 & 0 & 0\\
0 & -2.313 & 0.159 & 0 & 0 & 0 & 1.56 & 0.211 & 0 & 0\\
0 & -0.15 & -1.49 & 0 & 0 & 0 & 0.211 & -0.181 & 0 & 0\\
0 & 0 & 0 & -1.383 & -0.068 & 0 & 0 & 0 & 0.0096 & -0.061\\
0 & 0 & 0 & -0.068 & -1.383 & 0 & 0 & 0 & -0.061 & 0.0096
\end{array}\right)
\end{array}.
$$

TABLE II. Additional input parameters for two-fermion term. All numbers are in units of eV. Bold denotes values tuned to match experiment.

Charge transfer	Crystal field			Spin-orbit coupling			Magnetic field
Δ_{ct}	$\Delta 10D_q$	Δd_{xy}	$\Delta d_{xz}/d_{yz}$ mixing	ζ_i	ζ_n	ζ_c	H
0.8	**0.23**	**0.27**	**−0.06**	0.035	0.047	5.667	0.015

Since hopping depends on how electronic wave functions are spread between different atoms, it is only weakly influenced by strongly correlated physics and DFT generally captures the magnitude of hopping reasonably accurately. For this reason, we consider the off-diagonal interorbital hopping values to be good estimates for the true values. However, it was necessary to adjust the diagonal (crystal field) terms as DFT includes Coulomb interactions at the mean-field level, so the on-site energies are subject to double-counting errors, which we need to avoid. In order to fit the data we therefore add a further splitting between the Cr e_g and t_{2g} orbitals, denoted as $\Delta 10D_q$. The energy levels of the Cr and ligand states are also adjusted by adding an energy offset between the metal and ligand orbitals. This energy offset has the effect of tuning the charge transfer energy Δ_{ct}, which is defined as the cost to move a hole from the metal d orbitals onto the lowest energy ligand orbital. Δ_{ct} was calculated by diagonalizing the Hamiltonian with Cr-ligand hopping set to zero and then taking the energy difference between the d^3 and $d^4\underline{L}$ states (where $\underline{L}$ denotes a ligand hole).

The crystal field levels of the t_{2g} orbitals were also adjusted to reproduce the splitting in the lowest energy part of the experimental spectra. Since all of the d levels are in principle independent due to the low symmetry, there are multiple parameter choices which can place peaks at the energies matching the experimental spectra. The parameter choice which we found best matched the peak intensities was obtained by adjusting only the t_{2g} levels. The d_{xy} energy was shifted up by 0.27 eV, and the off-diagonal mixing term for d_{xz} and d_{yz} was decreased by 0.06 eV.

A small magnetic field of 15 meV, which splits the high spin $S \approx 3/2$ ground state into four nondegenerate levels, was introduced to mimic the environment in the ferromagnetically ordered layers. As a result, there were four free parameters in the two-fermion term: the Δd_{xy}, $\Delta d_{xz}/d_{yz}$ mixing, and $10D_q$ terms splitting the Cr d orbitals, and the splitting between the metal and the ligand orbitals parametrized as Δ_{ct}.

In summary, our calculation used three free parameters to fit the main features: an offset to the octahedral crystal field splitting $\Delta 10Dq$, the Coulomb scaling parameter k_{dd} (which scales with the Hund's coupling), and the charge transfer energy (Δ_{ct}). These parameters (indicated in bold in Tables I and II) were adjusted to best match the experimental RIXS spectra, while all other parameters were fixed to the specified values. Two additional parameters were then used to adjust the splitting of the t_{2g} orbitals to better match the finer structure in the low energy peak; however, we were not able to fully constrain these parameters based on the available data. Once the Hamiltonian was diagonalized, the RIXS and XAS cross sections were calculated for the experimental geometry and polarization settings. An inverse core-hole lifetime broadening of $\Gamma_c = 0.6$ eV and final state inverse lifetime of $\Gamma_f = 0.03$ eV were used.